OMAE2014-23302

WAVE-INDUCED ACCELERATIONS OF A FISH-FARM ELASTIC FLOATER: EXPERIMENTAL AND NUMERICAL STUDIES

Peng Li [*]
Department of Marine Technology
NTNU
NO-7491 Trondheim, Norway
Email: peng.li@ntnu.no

Odd M. Faltinsen
Centre for Autonomous Marine
Operations and Systems (AMOS),
Department of Marine Technology, NTNU
NO-7491 Trondheim, Norway
Email: Odd.faltinsen@ntnu.no

Marilena Greco
Centre for Autonomous Marine Operations
and Systems (AMOS), Department
of Marine Technology, NTNU
NO-7491 Trondheim, Norway
& CNR-INSEAN, The Italian Model Basin,
Rome, Italy
Email: marilena.greco@ntnu.no

ABSTRACT

Numerical simulations and experiments of an elastic circular collar of a floating fish farm are reported. The floater model without netting structure is moored with nearly horizontal moorings and tested in regular deep-water waves of different steepnesses and periods without current. Local overtopping of waves were observed in steep waves. The focus here is on the vertical accelerations along the floater in the different conditions. The experiments show that higher-order harmonics of the accelerations matter. A 3D weak-scatter model with partly nonlinear effects as well as a 3D linear frequency-domain method based on potential flow are used. From their comparison against the measurements, strong 3D and frequency dependency effects as well as flexible floater motions matter. The weak-scatter model can only partly explain the nonlinearities present in the measured accelerations.

INTRODUCTION

Fishery aquaculture in the open seas plays an increasingly important role, and it is believed to be a very efficient farming technique for the future. However, fish escape is a major problem for the industry. One reason is structural failure. An example is that contact between the net and chains connecting the floater and a bottom ring can cause rupture of the net. The fact that the net is considerably deformed in strong current matters. Further, a not properly designed bottom ring may considerably deform in severe weather conditions and damage the net.

High flexibility of netting, floating collar and sinker tube and their structural interaction are important effects. Bardestani and Faltinsen [1] discussed wave and current loads on the floater, netting and sinker tube of a section of a floating fish farm. Large snap loads due to the elastic behaviour of the net structure and the relative motion between the floater and the net are observed experimentally and predicted numerically.

Present investigation aims to provide further contribution in addressing critical conditions for fish-farms by focusing on the wave induced accelerations on the floater. Our experimental studies are related to a fish farm with a circular plastic collar made of high-density polyethylene (HDPE) pipes. The floater is a torus moored with a simplified horizontal mooring system. In reality, it is more common to use two concentric tori. The interaction with other parts of the fish farm, such as the netting structure, bottom rings, chains, ropes and a realistic mooring system, are important but are not studied. Both waves and current loads matter but current is neglected. For the examined problem, hydroelasticity matters due to the relatively small flexural rigidity of the floater and resonances are possible due to high-order wave load excitation. Engineering tools usually estimate

Copyright © 2014 by ASME

the floater response based on strip theory with linear potential flow and drag-force corrections from Morison equation, which disregards important 3D flow, frequency dependency, as well as nonlinear effects in steep waves. For example, Morisons equation is used in the analytical method proposed by Dong *et al.* [2] to estimate the elastic deformations of a semi-submerged torus in waves. Here the relevance of these parameters is examined through a synergic experimental and numerical analysis. In the next section the model tests are outlined, then the two adopted numerical solvers are described and the physical investigation is carried out. Main conclusions and further steps are drawn in the last section.

EXPERIMENTS

Model tests were performed in the Marine Cybernetics Laboratory at NTNU of Trondheim in January 2013. An objective was to measure the vertical accelerations along the floater. Since gravity waves are involved in the experiments, Froude scaling must be applied. Reynolds number scaling associated with vis-

cous effects can, therefore, not be satisfied. When flow separation does not happen, viscous effects are associated with the boundary layer flow and negligible relative to potential-flow effects. Moreover, since the Keulegan-Carpenter number is always small in our studies, the wave force amplitude will be dominated by potential-flow effects. However, we cannot outrule that viscous damping matters in case of flow separation. The latter may occur in steep waves with overtopping, as demonstrated in 2D numerical studies of a semi-submerged circular cylinder in waves by Kristiansen and Faltinsen [3].

The experimental set-up is illustrated in Fig. 1 and other parameters are shown in Table 1. The wave tank is 40m long, 6.45m wide, and 1.5m deep. It is equipped with a towing carriage, a flap piston wave maker and a damping beach covered by a rough, porous mat to increase its energy dissipation ability. The wave maker is controlled by software, which applies linear wave maker theory to estimate the necessary stroke of the piston for generating waves with a given height and period. A model test scale is 1 : 25 was used for the floater. Special attention was paid to the structural bending stiffness. The parameters were chosen
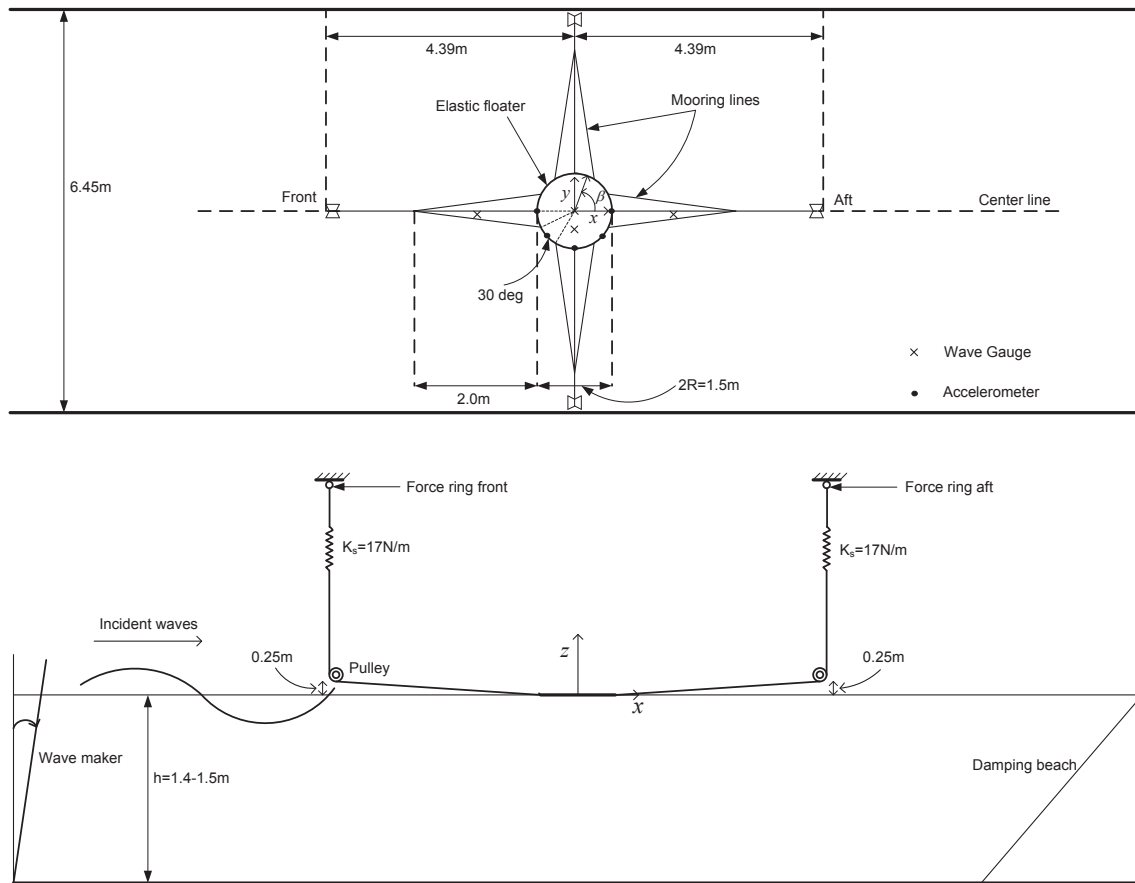

FIGURE 1: EXPERIMENTAL SET-UP. UPPER: TOP VIEW; LOWER: SIDE VIEW.

2   Copyright © 2014 by ASME

TABLE 1: DIMENSIONS USED IN THE EXPERIMENTS. MODEL SCALE 1 : 25.

Description	Parameter	Model scale	Full scale
Floater diameter	$D = 2c$	1.5m	37.5m
Cross-sectional diameter of floater	$2a$	38mm	0.95m
Floater bending stiffness	EI	0.464Nm^2	4.53×10^6Nm^2
Spring stiffness	k_s	17N/m	10.63kN/m

from typical values for existing collars. *EI* was estimated by using the static deflection equation $W = FL^3/3EI$ of a cantilever beam of length L and with a fixed end support at one end and load F applied at the other end of the beam. *EI* follows then from measuring the deflection W. A typical HDPE type plastic has a Young's modulus of elasticity $E \approx 1000MPa$. This model scale gave a realistic bending stiffness for the model. The floater was attached to the stationary carriage in the middle of the tank by means of four identical nearly horizontal mooring lines, at front, aft and laterally. They were connected to the floater through 12 attachment points with an equal interval of 30 deg. Springs with stiffness $k_s = 17N/m$ were used to connect the floater and the carriage. This corresponds to almost half of full scale spring stiffness ($27kN/m$) by Froude scaling. The pre-tension was $T_p = 5N$. The high pre-tension was needed to avoid slack due to large horizontal motion when testing large wave steepnesses and long wave periods. The elastic floater model was made from a corrugated tube used to cover electric cables in houses. Constant cross-section of the floater was obtained by covering the corrugation with waterproof adhesive electrical tape. The floater was semi-submerged in calm conditions. The vertical accelerations were measured by accelerometers at five points with an equal interval of $\pi/4$, starting from the front of the floater. Four wave gauges were used to measure the wave elevation.

Incident waves with wave height-to-wave length ratios $H/\lambda = 1/120, 1/60, 1/30$ and $1/15$ were tested. The wave period $T = 2\pi/\omega$ varied within $[0.6, 1.6]s$ with a step of $0.05s$. Here ω is the circular frequency. All test cases were repeated three to four times. A waiting time of 3 minutes between each test was chosen to damp out waves. In general, nearly steady-state conditions are reached after 10 wave periods. The time-series results in a selected window were band-passed filtered between lower and upper cut-off frequencies in order to remove high-frequency noise. The Hilbert transform was used for calculating instantaneous attributes of the resulting time series, *e.g.* the amplitude and frequency to describe the envelope curve of filtered measurements [4–6]. Eventually, the mean values, representing the amplitude of the measurements, and the standard deviations of the envelope curves were obtained.

Large vertical and horizontal motions with significant flexible effects, as well as waves over-topping the floater, were observed in several tests so, to properly examine the nonlinear features of the phenomena, first, second, third and fourth order harmonics of the measured acceleration signals were estimated.

NUMERICAL SOLVERS

Two theoretical potential-flow methods are applied. One method generalizes the weak-scatter model (Greco and Lugni [7]) with original theory due to Pawlowski [8]. Nonlinear effects are partly considered. The other method considers only linear frequency-domain effects. Elastic torus motions are accounted for in both methods. Empirical viscous drag loads may be added in the weak-scatter model. As in the model tests, both methods assume no current.

We discuss first the rigid-motion analysis of the floater in the weak-scatter model. A body-fixed Cartesian coordinate system $Ox_By_Bz_B$ with origin in the center of gravity (COG) of the torus and an inertial Cartesian coordinate system $Oxyz$ are introduced. When the floater is at rest, the x_B, y_B and z_B-axes are parallel with the x, y and z-axes, respectively. Further, the COG at rest is right above or below the origin of the $Oxyz$ system. The z-axis coincides with the torus axis and is vertical with positive direction upwards. The mean free surface is at $z = 0$. The incident regular waves propagate along the x-axis and are described by a second-order Stokes theory in deep water. When the torus is at rest in calm water, the torus is semi-submerged. The translatory rigid body-velocity components of the COG along the x_B, y_B and z_B-axes are U_1, 0 and U_3, respectively. The angular velocity component along the y_B-axis is q. The equations of rigid-body motions of the torus following from Newtons second law are expressed as [9]:

$$M\left(\dot{U}_1 + qU_3\right) = F_1 + Mg\sin\Theta,$$
$$M\left(\dot{U}_3 - qU_1\right) = F_3 - Mg\cos\Theta, \qquad (1)$$
$$I_{55}\dot{q} = F_5$$

Here M, I_{55}, g and Θ are the structural mass, pitch moment of inertia, acceleration of gravity and pitch angle, respectively. Further, F_1 and F_3 are external force components along the x_B and z_B-axes, respectively. F_5 is external moment about the y_B-axis. The external loads are due to the mooring, nonlinear hydrostatic

3 Copyright © 2014 by ASME

and Froude-Kriloff loads as well as hydrodynamic loads associated with flow caused by the torus velocity and scattering of the incident waves. The hydrodynamic loads are consistent within linear theory but include nonlinear effects due to satisfaction of the body-boundary conditions. We denote the surge and heave displacements of the torus along the x and z-axes as η_1 and η_3, respectively. The following differential equations link rigid-body velocity components, angular velocity, displacements and pitch angle [9]:

$$\frac{d\eta_1}{dt} = U_1 \cos\Theta + U_3 \sin\Theta,$$
$$\frac{d\eta_3}{dt} = -U_1 \sin\Theta + U_3 \cos\Theta, \qquad (2)$$
$$\frac{d\Theta}{dt} = q.$$

The flexible vertical (w) and lateral (radial, v_r) torus motions are described by the following modified beam equations with tension and radius of curvature effects:

$$m\frac{\partial^2 w}{\partial t^2} + EI\frac{\partial^4 w}{\partial s^4} - \frac{\partial}{\partial s}\left(T_{as}\frac{\partial w}{\partial s}\right)$$
$$= f_3^{\text{FK}+\text{hydrostatic}} + f_3^{\text{hydrodynamic}} + f_3^{\text{str.}+\text{mooring}} \qquad (3)$$

$$m\frac{\partial^2 v_r}{\partial t^2} + EI\left(\frac{\partial^4 v_r}{\partial s^4} + \frac{1}{c^2}\frac{\partial^2 v_r}{\partial s^2}\right) - \frac{\partial}{\partial s}\left(T_{as}\frac{\partial v_r}{\partial s}\right)$$
$$= f_r^{\text{FK}+\text{hydrostatic}} + f_r^{\text{hydrodynamic}} + f_r^{\text{str.}+\text{mooring}} \qquad (4)$$

Here the differentiation $\partial/\partial s = c^{-1}\partial/\partial\beta$ is along the torus where β is defined in Fig. 1. m is the floater mass per unit length and EI is the bending stiffness and T_{as} is the axial stiffness following from a static analysis of the moored floater. Further, $f_3^{\text{FK}+\text{hydrostatic}}$ and $f_r^{\text{FK}+\text{hydrostatic}}$ are the vertical and radial nonlinear hydrostatic and Froude-Kriloff forces per unit length and $f_3^{\text{hydrodynamic}}$ and $f_r^{\text{hydrodynamic}}$ are the vertical and radial hydrodynamic forces per unit length due to the floater velocity and scattering of the incident waves. Finally, $f_3^{\text{str.}+\text{mooring}}$ and $f_r^{\text{str.}+\text{mooring}}$ describe the effect of structural damping and mooring. The flexible vertical and radial motions are expressed as:

$$w = \sum_{n=2}^{\infty} a_n(t)\cos(n\beta)$$
$$v_r = \sum_{n=2}^{\infty} b_n(t)\cos(n\beta) \qquad (5)$$

The nonlinear hydrostatic and Froude-Kriloff loads involve pressure integration on the instantaneous wetted surface. The latter is found by approximating the free-surface elevation at the floater as the incident wave elevation. The effect of rigid-body and elastic floater motions is considered. Both over-topping and dry cross-sections may occur due to large relative vertical floater

motion. The difference between the water pressure and the atmospheric pressure on the instantaneous position of the floater is $-\rho g z + p_1$ with $p_1 = -\rho\partial\varphi_0/\partial t - \rho \mid \bigtriangledown\varphi_0\mid^2/2$ when $z \leq 0$ and $p_1 = -\rho\partial\varphi_0/\partial t$ when $z > 0$. Here φ_0 is the incident wave potential.

The hydrodynamic loads are represented in terms of convolution integrals with retardation functions in a similar manner as Cummins [10] described for linear rigid-body velocities. A modification is that scattering is included. The free-surface condition for the velocity potential φ is $\partial^2\varphi/\partial t^2 + g\partial\varphi/\partial z = 0$ on $z = 0$. The fact that the body boundary condition $\partial\varphi/\partial n = (\mathbf{V}_{\text{floater}} - \mathbf{V}_{\text{wave}})\cdot\mathbf{n}$ is applied on the instantaneous floater position leads to nonlinear effects. Here $\mathbf{V}_{\text{wave}}$ is the incoming-wave velocity, $\mathbf{V}_{\text{floater}}$ is the floater velocity and $\mathbf{n}$ is the body normal vector. The frequency-domain added mass and damping coefficients needed in calculating the retardation functions follow by satisfying the body-boundary conditions on the mean oscillatory position and properly integrating linear hydrodynamic pressure. The linear potential-flow frequency-domain panel code WAMIT was used for both flexible and rigid-body modes.

The effect of mooring on $f_3^{\text{str.}+\text{mooring}}$ is small and neglected. Since we do not know the structural damping associated with the different flexible modes, the following strategy is tried out. A damping of the form $[p_1 + \triangle p\cdot(j-1)]B_{cr,j}$, is assumed for each vertical and radial flexible mode j, with $B_{cr,j}$ the corresponding critical damping, $p_1 = 0.05$ and $\triangle p = 0.01$. With this formula a structural damping equal to the 5% of the critical damping is used for the first flexible vertical (radial) mode and increased with a step of 1% with the number of mode. This arbitrary choice is qualitatively reasonable since it is expected a greater effect of the structural damping in limiting the higher modes. The comparison with a similar formula using $p_1 = 0.01$ gave very close results for the longer incident-wave cases while indicated higher-mode amplitudes much larger than observed in the physical case. The surge equation also includes a quadratic viscous drag term, which is found from free-decay tests in the present study.

The other method is a frequency-domain linear theory. Only vertical motions are analysed and $f_3^{\text{str.}+\text{mooring}}$ is set equal to zero. Eqn. (3) is written as:

$$m\frac{\partial^2 w}{\partial t^2} + \rho g 2aw + EI\frac{\partial^4 w}{\partial s^4} - \frac{\partial}{\partial s}\left(T_{as}\frac{\partial w}{\partial s}\right)$$
$$= f_3^{\text{added mass}+\text{damping}} + f_3^{\text{wave excit}} \qquad (6)$$

Since rigid-body heave and pitch are included, we write:

$$w = \sum_{n=0}^{\infty} a_n(t)\cos(n\beta) \qquad (7)$$

Here ρ is the mass density of water and g is the acceleration of gravity. $f^{\text{added mass}+\text{damping}}$ is the vertical added mass and damping force per unit length of the floater that includes frequency-dependent added mass $a_{33}^{(n)}$ and damping coefficients

4

$b_{33}^{(n)}$ associated with the different modes n. They are found by studying forced harmonic velocity $\dot{a}_n \cos(n\beta)$, multiplying the cross-sectional vertical linear hydrodynamic force with $c \cos(2\beta)$ and integrating with respect to β from 0 to 2π. The corresponding added mass and damping coefficients for the floater are $A_{33}^{(n)} = 2\pi c a_{33}^{(n)}$, $B_{33}^{(n)} = 2\pi c b_{33}^{(n)}$. Further, $f_3^{\text{wave excit}} = \sum_{n=0}^{\infty} f_{3,n}^{\text{wave excit}} \cos(n\beta)$ is the vertical wave excitation force on the floater per unit length that includes both the Froude-Kriloff force and the force due to scattering of the incident waves. Li and Faltinsen (2012) [11] used WAMIT and two smallfrequency slender-body theories to evaluate $f_3^{\text{added mass}+\text{damping}}$ and $f_3^{\text{wave excit}}$. The slender-body theories assume small νc and $\nu a = O(1)$ with $\nu = \omega^2/g$. Matched asymptotic expansion with near-field and far-field descriptions was applied. The slender-body theories differed in the way to calculate the scattering force: one method was based on a relative velocity concept; the other method generalized the Haskind relation. The different methods give quite similar predictions in our considered frequency range and show very strong 3D and frequency dependence implying that strip theory fails. The slender-body theories are clearly more computationally efficient than WAMIT.

The solution procedure of Eqns. (3), (4) and (6) is as follows. T_{as} is assumed constant and equal to $T_{as}^{(i)}$ between each mooring line. The values of $T_{as}^{(i)}$ used in the presented case studies are $\left[T_{as}^{(1,3,5,7)}, T_{as}^{(2,4,6,8)}\right] = [0.4108, 0.7071] \times T_p$, where T_p is the pre-tension of the mooring lines.

Within the linear method, Eqn. (7) is substituted into Eqn. (6), which is multiplied by $\cos(m\beta)$ and integrated from 0 to 2π. Then, the equations of motion become:

$$\left(m + a_{33}^{(m)}\right)\ddot{a}_m + b_{33}^{(m)}\dot{a}_m + \left(\rho g 2a + \frac{EI}{c^4}m^4\right)a_m$$
$$+ \frac{1}{\alpha_m \pi c^2} \sum_{n=0}^{\infty} \sum_{i=1}^{8} n^2 T_{as}^{(i)} \int_{\beta_i}^{\beta_{i+1}} \cos(n\beta)\cos(m\beta)\,\mathrm{d}\beta\, a_n \quad (8)$$
$$= f_{3,m}^{\text{wave excit}}$$

for the unknown amplitudes a_m. Here $\alpha_0 = 2$, and $\alpha_m = 1$, $m \geq 1$. Further, β_i and β_{i+1} are the end angles β for a torus segment between two successive mooring lines attached to the floater. There are eight of such segments. Since $\ddot{a}_m = -\omega^2 a_m$ and $\dot{a}_m = -i\omega a_m$ with time dependence $exp(-i\omega t)$, Eqn. (8) are not true differential equations. The Eqn. (8) show that the axial tension provides coupling between the different modes.

The weak-scatter model follows a similar procedure in re-expressing the vertical and radial modified beam equations for the flexible modes by multiplying them with $\cos(m\beta)$ and integrating from 0 to 2π. This leads to an equation system for the unknowns a_m and b_m. The weak-scatter equations are solved numerically in time using a fourth-order Runge-Kutta scheme.

The resulting weak-scatter solver is quite efficient if compared with more general fully-nonlinear potential-flow methods since it requires in time only the discretization of the instantaneous wetted body surface, the estimation of nonlinear Froude-Kriloff and hydostatic loads and the satisfaction of the nonlinear body-boundary condition in the hydrodynamic problem. Further, if plunging breakers occur, a fully-nonlinear potential-flow method has limitations. The geometry of the floater and its elastic behaviour lead however to challenges in terms of numerical efficiency and accuracy. Some important reasons are: 1) the geometry involves two quite different spatial scales, with the cross-sectional radius a typically much smaller than the global radius c of the floater; 2) the elastic behaviour leads to the need of a larger number of degrees-of-freedom to be accounted for; 3) the floater is associated with long-time memory effects, which mean that the convolution integrals must be estimated for a time interval typically large. Fig. 2 presents retar-
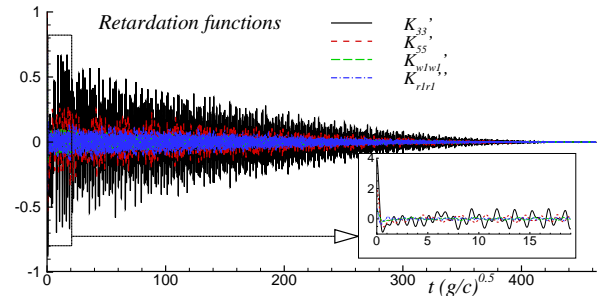
FIGURE 2: NON-DIMENSIONAL RETARDATION FUNCTIONS FOR HEAVE, PITCH, FIRST ELASTIC VERTICAL AND RADIAL MODES AS A FUNCTION OF TIME. THE ENLARGED VIEW SHOWS THE DETAIL OF THE BEHAVIOUR AT SMALL TIMES INTERVAL. $K_{33}' = K_{33}/(\rho gac)$, $K_{55}' = K_{55}/(\rho gac^3)$, $K_{w1w1}' = K_{w1w1}/(\rho ga)$, $K_{r1r1}' = K_{r1r1}/(\rho ga)$. ρ, g, a, c ARE DEFINED IN TABLE 1 AND TEXT.

dation functions in heave (K_{33}) and pitch (K_{55}) and retardation functions associated with the lowest vertical (K_{w1w1}) and radial (K_{r1r1}) flexible modes. Here $K_{jj}(t) = \frac{2}{\pi}\int_0^\infty B_{jj}(\omega)\cos(\omega t)\,\mathrm{d}\omega$ with $B_{33}(\omega)$ and $B_{55}(\omega)$ as frequency-domain damping coefficients in heave and pitch of the floater. Further, $K_{w1w1}(t) = \frac{2}{\pi}\int_0^\infty B_{33}^{(2)}(\omega)\cos(\omega t)\,\mathrm{d}\omega$, $K_{r1r1}(t) = \frac{2}{\pi}\int_0^\infty B_{rr}^{(2)}(\omega)\cos(\omega t)\,\mathrm{d}\omega$ where $B_{33}^{(2)}(\omega)$ has been previously defined and $B_{rr}^{(2)}(\omega)$ is associated with studying forced radial flexible mode velocity $\dot{b}_2(t)\cos(2\beta)$, multiplying the linear hydrodynamic cross-sectional radial force with $c\cos(2\beta)$ and integrating with respect to β from 0 to 2π. The retardation functions, both for rigid and elastic modes, become negligible for times larger than about $400\sqrt{c/g}$, corresponding to nearly 75 periods of the longest waves investigated here.

Actually, looking more closely at the behaviour for small times (see enlarged view in the figure), the retardation functions

5   Copyright © 2014 by ASME

for heave and pitch have the most important contributions for $t < 2\sqrt{c/g}$. This suggests that, if these rigid motions dominate the floater response, steady-state conditions would be reached quickly in time. Things are different for the first vertical and radial elastic modes. In this case the memory effects are of similar importance along the time axis, suggesting that steady-state conditions require longer time to be reached when these modes are important for the floater response. This behaviour of the retardation functions is very special and probably connected with the ring shape of the elastic body and the very complicated frequency dependency for added-mass and damping coefficients with several peaks and troughs, and occurrence of negative added mass and almost zero damping. It has been verified that using the retardation functions to calculate added mass and damping coefficients is consistent with added mass and damping coefficients calculated by WAMIT.

PHYSICAL INVESTIGATIONS

Convergence of the weak-scatter results has been checked in terms of spatial body discretization, time step and number of modes. It was found that 24 panels along the cross-sectional diameter and 988 panels along the global diameter of the floater were suitable to have nearly converged results. $\Delta t = 0.0025T$, with T the incident wave period, was confirmed to be a suitable time step. Ten vertical and ten radial flexible modes have been considered. Since the experiments are performed with horizontal mooring lines, a restoring is caused for the surge, sway and radial elastic modes. Using free-decay tests in surge with only the two mooring lines in x-direction, the restoring and damping for surge and sway (due to the symmetry of the body and of the mooring lines set-up) were obtained. In this way viscous-damping corrections were included in the simulations.

The method was applied to the cases with smallest, intermediate and largest incident-wave periods, *i.e.* $T = 0.6s$, $1.05s$ and $1.6s$. For longer incident waves rigid motions tend to dominate the floater response, so we can expect that steady-state conditions are reached sooner than for shorter waves. The numerics indicates that they are reached after $20T$ for the longest wave while the experiments show important variation between the measurements done after $20T$ and those made after $50T$. For $T = 1.05s$, steady-state conditions are nearly reached numerically and experimentally after $50T$, while both of them indicate a difficulty in reaching steady-state conditions for the shortest wave even after $100T$. This is consistent with the fact that in this case rigid motions are comparable with the elastic motions and can interact with them, so memory effects need longer times to die out. Globally the numerics tends to underestimate the physical vertical motions. This does not seem to be connected with the use of a too large structural damping for the elastic modes. The numerical results with two different structural damping strategies are identical for the two longer waves, as expected since the floater
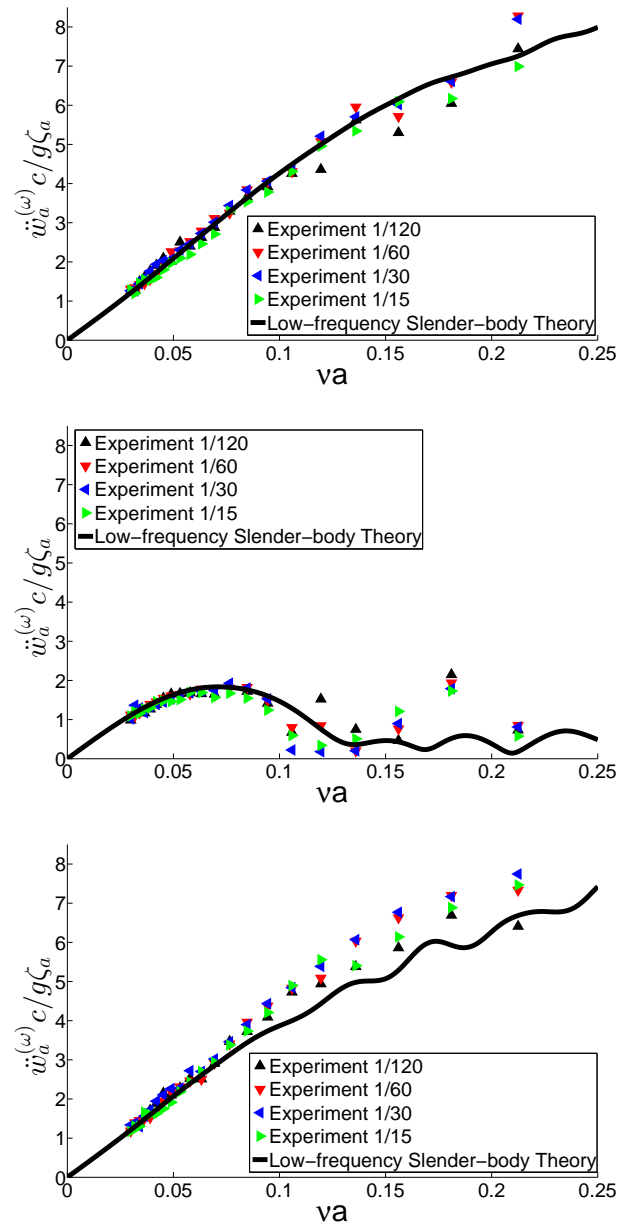

FIGURE 3: NON-DIMENSIONAL AMPLITUDES OF FIRST-HARMONICS FOR EXPERIMENTAL AND NUMERICAL VERTICAL ACCELERATION $\ddot{w}_a^{(\omega)}$ AT FRONT, LEFT AND AFT POSITIONS ON THE FLOATER FOR DIFFERENT WAVE STEEPNESSES AND FREQUENCIES.

response in this case is dominated by the rigid motions; moreover the reduction of the damping does not ameliorate the agreement with the experiments for the shortest wave.

Fig. 3 compares amplitudes of experimental and linear theoretical predictions of the first harmonics of vertical accelerations at the front, side and aft of the floater as a function of nondi-

6   Copyright © 2014 by ASME

TABLE 2: EXPERIMENTAL, WEAK-SCATTER AND LINEAR THEORY VALUES OF $\ddot{w}_a^{(\omega)} c/g\zeta_a$. $\ddot{w}_a^{(\omega)}$ IS THE AMPLITUDE OF THE FIRST HARMONICS OF VERTICAL ACCELERATIONS. c, g AND ζ_a ARE DEFINED IN TABLE 1 AND TEXT.

va	H/λ	Front				Left				Aft			
		Exp. μ	Exp. σ	Weak Scatter	Linear	Exp. μ	Exp. σ	Weak Scatter	Linear	Exp. μ	Exp. σ	Weak Scatter	Linear
0.0299	1/120	1.254	0.020	1.238	1.206	0.990	0.038	1.100	1.109	1.244	0.027	1.232	1.203
	1/60	1.308	0.036	1.224		1.114	0.015	1.089		1.185	0.027	1.218	
	1/30	1.257	0.026	1.194		1.016	0.029	1.062		1.340	0.033	1.186	
	1/15	1.298	0.033	1.148		1.097	0.030	0.903		1.157	0.038	1.094	
0.0694	1/120	2.874	0.085	2.846	2.958	1.668	0.061	1.735	1.834	2.939	0.066	2.905	2.849
	1/60	3.144	0.085	2.838		1.794	0.054	1.722		2.925	0.055	2.902	
	1/30	3.023	0.039	2.781		1.753	0.034	1.683		3.023	0.050	2.851	
	1/15	2.694	0.072	2.588		1.570	0.023	1.114		2.945	0.060	2.833	
0.2125	1/120	7.185	0.229	6.716	7.262	0.772	0.153	0.323	0.191	6.196	0.197	7.328	6.690
	1/60	8.261	0.194	6.713		0.838	0.147	0.327		7.298	0.182	7.325	
	1/30	8.266	0.177	6.686		0.809	0.219	0.338		7.757	0.150	7.293	
	1/15	6.722	0.611	6.663		0.508	0.229	0.502		7.223	0.678	7.281	

mensional squared frequency va and wave steepness. The low-frequency slender-body theory uses the relative velocity to calculate the scattering effect. Twenty-two modes are used. Increasing number of modes has a negligible effect. The low-frequency slender-body theory agrees, in general, satisfactorily with experiments. An exception is for the left part of the floater at $va = 0.181$. Weak-scatter results of the amplitude of the first harmonics of vertical accelerations at the front, side and aft of the floater are compared in Table 2 with experiments and the low-frequency slender-body theory for $va = 0.0299, 0.0694, 0.2125$ and different wave steepnesses. The table provides also information about the experimental mean value μ and standard deviation $\sigma = \left(\sigma_{ea}^2 + \sigma_{re}^2\right)^{0.5}$, where σ_{ea} is the standard deviation of each case due to the time-dependent amplitude variation and σ_{re} is the standard deviation due to repeating the tests three or four times for each wave condition. The relative error is defined as $\sigma/\mu \cdot 100\%$, where μ is the experimental mean value and σ is the total experimental standard deviation. Relative error caused by repetition was less than 1.0%. Thus, the obtained time series showed good repeatability.

The time series of the experimental accelerations obtained by filtering out higher harmonics than ω is shown in Fig. 4 for one test case with $H/\lambda = 1/15$ and $va = 0.0299$. The red envelope curve of the acceleration amplitude has been used to calculate μ and σ_{ea}. The physical reason to σ_{ea} is not fully known. The maximum relative error is respectively 9.1%, 45.1% and
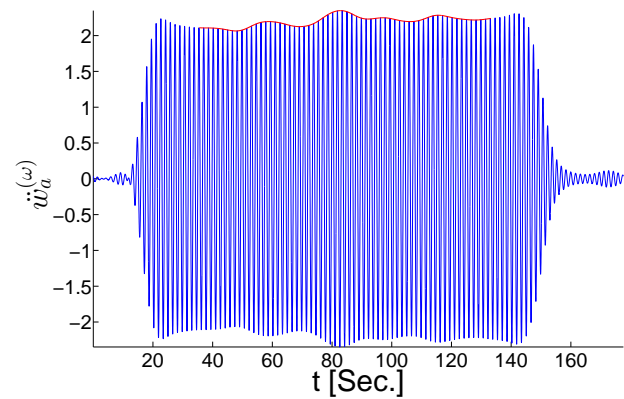

FIGURE 4: TIME SERIES OF THE FIRST HARMONICS OF EXPERIMENTAL VERTICAL ACCELERATIONS AT THE FRONT OF THE FLOATER WITH $H/\lambda = 1/15$ AND $T = 1.6s$.

9.4% at front, left and aft positions on the floater. However, there is in general a small relative error. Another error source is that the accelerometer is body-fixed and can only measure the acceleration in normal direction while the theories predict vertical accelerations. However, theoretical estimates of the latter effect showed a negligible error. The weak-scatter method agrees well with the experiments except for the left part of the floater when $va = 0.2125$. However, the acceleration level is small relative to values in the front and aft part of the floater. Both the
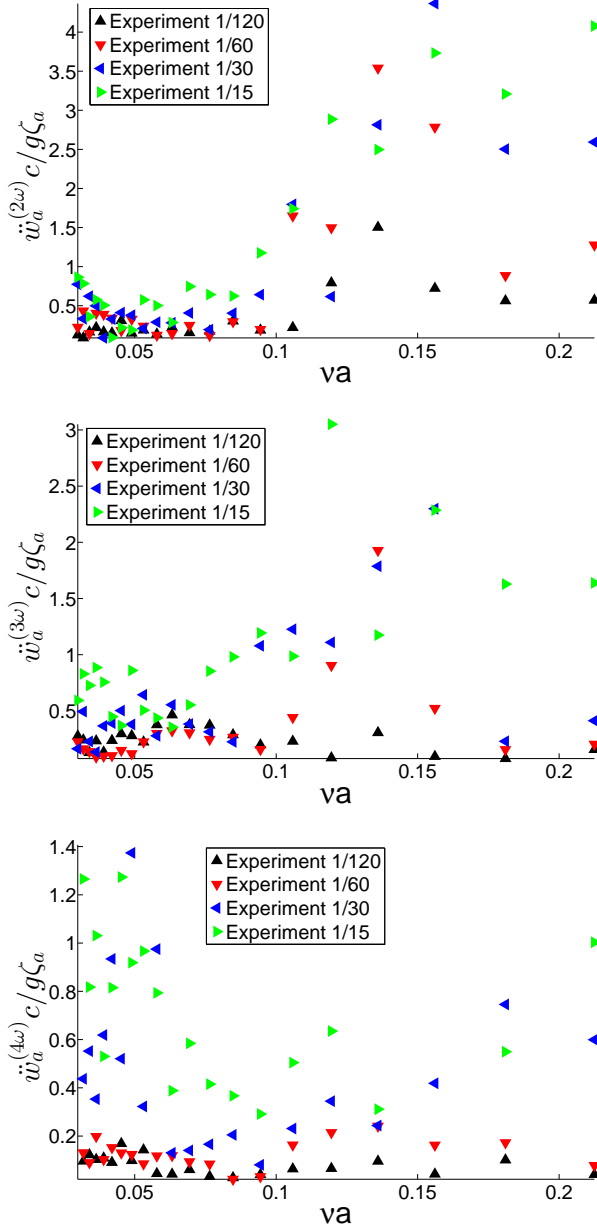
7

Copyright © 2014 by ASME

FIGURE 5: NON-DIMENSIONAL AMPLITUDES OF HIGHER-ORDER HARMONICS FOR EXPERIMENTAL VERTICAL ACCELERATION AT THE FRONT OF THE FLOATER FOR DIFFERENT WAVE STEEPNESSES AND FREQUENCIES. $\ddot{w}_a^{(2\omega)}$, $\ddot{w}_a^{(3\omega)}$ AND $\ddot{w}_a^{(4\omega)}$ ARE THE AMPLITUDES OF THE SECOND, THIRD AND FOURTH HARMONICS OF VERTICAL ACCELERATIONS.

weak-scatter method and the experiments show a small nonlinear dependence on the incident wave amplitude.

The amplitudes of the second, third and fourth harmonics of measured vertical accelerations of model tests at the front of the

TABLE 3: PREDICTED UNDAMPED NATURAL FREQUENCIES IN rad/s FOR VERTICAL MODES.

22.61	23.11	23.49	23.99	24.33	25.15	25.67
25.83	26.11	26.73	26.97	27.49	28.21	28.61
28.93	29.37	29.63	30.11	30.31	30.83	30.99
31.32	31.75	32.17	32.29	32.61	32.81	33.01
33.11	33.45	33.54	33.73	34.07	34.33	34.67
34.76	34.93	35.16	35.27	35.35	35.53	35.85
35.95	36.11	36.41	36.53	36.67	36.88	36.97
37.09	37.23	37.42	37.53	37.65	37.79	38.03
38.21	38.33	38.51	38.61	38.75	38.87	39.04
39.15	39.28	39.39	39.57	39.67	39.80	39.92
40.08	40.18	40.32	40.43	40.59	40.64	40.94
41.10	41.20	41.34	41.44	41.59	41.70	41.83
42.08	42.21	42.32	42.57	42.66	42.81	43.05
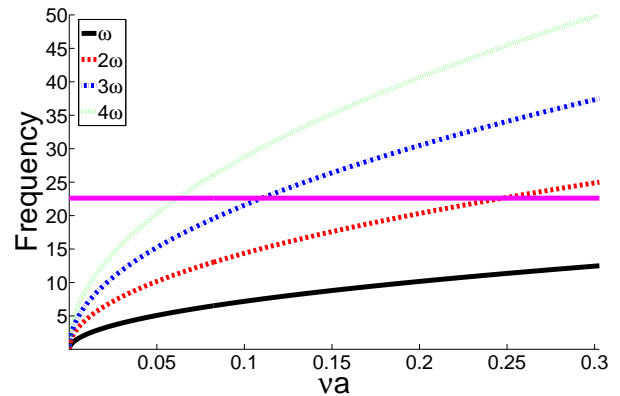
FIGURE 6: FREQUENCIES ω, 2ω, 3ω AND 4ω IN rad/s AS A FUNCTION OF $va = \omega^2 a/g$. THE LOWER BOND FOR THE NATURAL FREQUENCIES OF VERTICAL MODES IS INDICATED WITH THE HORIZONTAL PINK LINE.

floater are presented in Fig. 5 as a function of nondimensional squared frequency va and wave steepness. The values are by no means negligible relative to the first harmonic part presented in Fig. 3 except, in general, for the smallest wave steepness. One reason may be over-topping of waves which was evident in the front and aft parts for wave steepnesses 1/30 and 1/15. Another reason may be that higher-harmonic wave loads have excited resonant oscillations. Table 3 lists predicted undamped natural frequencies for different vertical modes. It increases from left to right in each row and up to the largest value of 4ω in

8

Copyright © 2014 by ASME

TABLE 4: EXPERIMENTAL AND WEAK-SCATTER VALUES OF $\ddot{w}_a^{(2\omega)}c/g\zeta_a$. $\ddot{w}_a^{(2\omega)}$ IS THE AMPLITUDE OF THE SECOND HARMONICS OF VERTICAL ACCELERATIONS.

va	H/λ	Front			Left			Aft		
		Experiment μ	Experiment σ	Weak Scatter	Experiment μ	Experiment σ	Weak Scatter	Experiment μ	Experiment σ	Weak Scatter
0.0299	1/120	0.126	0.051	0.070	0.090	0.027	0.013	0.157	0.054	0.065
	1/60	0.224	0.084	0.130	0.096	0.044	0.044	0.210	0.081	0.124
	1/30	0.774	0.057	0.220	0.097	0.037	0.093	0.449	0.066	0.237
	1/15	0.865	0.119	0.296	0.238	0.041	0.217	0.726	0.080	0.324
0.0694	1/120	0.155	0.068	0.175	0.042	0.026	0.051	0.143	0.063	0.186
	1/60	0.248	0.048	0.333	0.042	0.025	0.102	0.106	0.034	0.352
	1/30	0.407	0.043	0.501	0.084	0.033	0.198	0.147	0.033	0.511
	1/15	0.746	0.103	1.396	0.968	0.099	0.553	0.691	0.069	1.207
0.2125	1/120	0.570	0.136	0.474	0.175	0.086	0.300	0.508	0.097	0.497
	1/60	1.277	0.442	1.016	0.979	0.166	0.683	2.074	0.192	1.045
	1/30	2.593	0.606	2.305	1.255	0.569	1.731	5.864	0.546	2.267
	1/15	4.078	1.091	1.933	2.463	0.855	4.044	5.311	0.973	1.397

the model tests. There are 91 natural frequencies from the first one $22.61\,rad/s$ to $43.05\,rad/s$. The very strong frequency dependency of generalized added mass for vertical modes causes a small interval between successive natural frequencies. Fig. 6 presents frequencies ω, 2ω, 3ω and 4ω in rad/s as a function of $va = \omega^2 a/g$. The pink solid straight line is the first natural frequency $22.61\,rad/s$. When ω, 2ω, 3ω and/or 4ω is above the pink line for a given va, it indicates that resonant oscillations may occur depending on the magnitude of the generalized excitation force and damping. If we relate this fact to the experimental results in Fig. 5, we note that not all large higher harmonic accelerations can be explained to be a consequence of resonance.

The amplitude of the second harmonics of vertical accelerations from experiments and by the weak-scatter method are compared in Table 4 for the same va as in Table 2. The relative experimental errors shown in Table 2 and 4 are large for some wave conditions. As discussed already, relative error caused by repetition was negligible. Thus, the main contribution comes from the time variation of amplitude. The maximum relative error is respectively 43.6%, 61.1% and 44.0% at front, left and aft positions on the floater. The weak-scatter method has a reasonable agreement with experiments for wave steepnesses 1/120, 1/60 and 1/30. The difference is larger for the highest wave steepness 1/15. Predicted values of the amplitude of the third and

fourth harmonics of accelerations by the weak-scatter model for and different wave steepnesses were very low relative to the experimental results shown in Fig. 5.

The experimental error is of same order of magnitude as for the amplitude of the second harmonics of the accelerations. When linear effects dominate, the two considered potential-flow methods are rational. However, the calculated effect of axial tension on flexible modes are approximated by using constant tension between each mooring-line attachment points. When nonlinear hydrostatic and Froude-Kriloff loads dominate, the weak-scatter model is partially rational. An error source is that the local free-surface elevation influenced by the flow caused by torus velocities and scattering has not been used in finding the wetted surface. Since the semi-submerged torus surface is not vertical in the free-surface zone, it is impossible with the considered method to find the local free-surface elevation.

The weak-scatter model has similarities with blended methods used in calculating springing and whipping of ships. Shao and Faltinsen [12] documented that blended methods do not predict the fact that the second-order potential due to full hydrodynamic interaction between the incident waves and the ship gives dominant contribution to sum-frequency hydrodynamic loads which is also a well-known fact for TLPs. The weak-scatter model does not handle the effect of flow separation in a ratio-

Copyright © 2014 by ASME

nal way. Kristiansen and Faltinsen [13] demonstrated by the CIP method that flow separation occurs during over-topping of waves on a semi-submerged circular cross-section.

Since higher-order harmonics of wave loads can cause resonant excitation of flexible modes, structural damping may matter. We do not know what the structural damping was for the different modes of the tested structure and, therefore, what the error due to structural damping was in the weak-scatter model.

CONCLUSIONS

Model tests of an elastic circular floater of a fish farm have been conducted to measure the vertical accelerations along the floater in regular waves of different steepnesses and periods. A nonlinear weak-scatter method and a linear frequency-domain method have been applied to complement the physical tests. The analysis showed that flexible motions, 3D flow and frequency dependency are important. Wave overtopping may occur in steeper waves. Good agreement was achieved for the first harmonic component of vertical accelerations at front, side and aft positions on the floater. Important higher-order harmonic components of experimental accelerations occur. The second harmonic acceleration component is well predicted by the weak-scatter method for wave steepnesses 1/120, 1/60 and 1/30. The differences are larger for the highest wave steepness 1/15. Predictions of third and fourth harmonic acceleration components are less satisfactory. It is speculated if higher-order wave loads may cause resonant vertical accelerations of the floater. A next step is to include a net cage with bottom weights and study the wave-induced vertical accelerations and structural stresses of the floater including practical consequences.

REFERENCES

[1] Bardestani, M., and Faltinsen, O. M., 2013. "A Two-Dimensional Approximation of a Floating Fish Farm in Waves and Current with the Effect of Snap Loads". In Proceedings of the ASME 2013 32nd International Conference on Ocean, Offshore and Arctic Engineering. OMAE2013-10487.

[2] Dong, G. H., Hao, S. H., Zhao, Y. P., Zong, Z., and Gui, F. K., 2010. "Elastic Responses of a Flotation Ring in Water Waves". *Journal of Fluids and Structures,* **26**(1), pp. 176–192.

[3] Kristiansen, D., and Faltinsen, O. M., 2008. "Wave Loads on Floaters of Aquaculture Plants". In Proceedings of the ASME 27th International Conference on Offshore Mechanics and Arctic Engineering. OMAE2008-57084.

[4] Claerbout, J. F., 1976. *Fundamentals of Geophysical Data Processing*. McGraw-Hill.

[5] Marple, S. L., 1999. "Computing the Discrete-Time Analytic Signal via FFT". *IEEE Transactions on Signal Processing,* **47**(9), September, pp. 2600–2603.

[6] Oppenheim, A. V., and Schafer, R. W., 1998. *Discrete-Time Signal Processing*. Prentice-Hall.

[7] Greco, M., and Lugni, C., 2012. "3-D Seakeeping Analysis with Water on Deck and Slamming. Part 1: Numerical Solver". *Journal of Fluids and Structures,* **33**, pp. 127–147.

[8] Pawlowski, J. S., 1991. "A Theoretical and Numerical Model of Ship Motions in Heavy Seas". In SNAME Transactions, Vol. **99**, pp. 315–319.

[9] Faltinsen, O. M., 2005. *Hydrodynamics of High-Speed Marine Vehicles*. Cambridge University Press.

[10] Cummins, W. E., 1962. "The Impulse Response Function and Ship Motions". *Symposium on Ship Theory, Schiffstechnik,* **9**, pp. 101–109.

[11] Li, P., and Faltinsen, O. M., 2012. "Wave Induced Response of an Elastic Circular Collar of a Floating Fish Farm,". In Proceedings of 10th International Conference on Hydrodynamics, Vol. **2**, pp. 58–64.

[12] Shao, Y. L., and Faltinsen, O. M., 2012. "A Numerical Study of the Second-order Wave Excitation of Ship Springing in Infinite Water Depth". *Journal of Engineering for the Maritime Environment,* **226**(2), pp. 103–119.

[13] Kristiansen, D., and Faltinsen, O. M., 2009. "Non-linear Wave-induced Motions of Cylindrical-shaped Floaters of Fish Farms". *Journal of Engineering for the Maritime Environment,* **223**(3), pp. 361–375.